ARTICLE OPEN

Check for updates

Elemental partitioning and corrosion resistance of Ni–Cr alloys revealed by accurate ab-initio thermodynamic and electrochemical calculations

Liang-Feng Huang [1,2], Yusi Xie[3], Karl Sieradzki[3] and James M. Rondinelli [1]✉

Elemental partitioning during thermal processing can significantly affect the corrosion resistance of bulk alloys operating in aggressive electrochemical environments, for which, despite decades of experimental and theoretical studies, the thermodynamic and electrochemical mechanisms still lack accurate quantitative descriptions. Here, we formulate an ab initio thermodynamic model to obtain the composition- and temperature-dependent free energies of formation ($\Delta_f G$) for Ni–Cr alloys, a prototypical group of corrosion-resistant metals, and discover two equilibrium states that produce the driving forces for the elemental partitioning in Ni–Cr. The results are in quantitative agreement with the experimental studies on the thermodynamic stability of Ni–Cr. We further construct electrochemical (potential–pH) diagrams by obtaining the required $\Delta_f G$ values of native oxides and (oxy)hydroxides using high-fidelity ab-initio calculations that include exact electronic exchange and phononic contributions. We then analyze the passivation and electrochemical trends of Ni–Cr alloys, which closely explain various oxide-film growth and corrosion behaviors observed on alloy surfaces. We finally determine the optimal Cr content range of 14–34 at%, which provides the Ni–Cr alloys with both the preferred heat-treatment stability and superior corrosion resistance. We conclude by discussing the consequences of these findings on other Ni–Cr alloys with more complex additives, which can guide the further optimization of industrial Ni–Cr-based alloys.

npj Materials Degradation (2023)7:94 ; https://doi.org/10.1038/s41529-023-00414-w

INTRODUCTION

Ni–Cr-based alloys, e.g., Inconel grades, bond-coat NiCrAlY, and Ni–Cr-based multiprincipal-element alloys, are deployed in diverse applications owing to their superior thermodynamic and kinetic stabilities, mechanical properties, and resistance against environmental attack[1–12]. Their additional irradiation resistance makes them the preferred metals used in modern nuclear-power reactors[13–16]. In addition, Cr also has its special significance in light-water reactors, because the Cr coating may prohibit the catastrophic catalytic reaction between Zr-based nuclear fuel cladding and environmental water[17–19]. It is the native oxides, hydroxides, and (oxy)hydroxides spontaneously formed on alloy surfaces that offer protection to the metal components from environmental degradation. For example, the corrosion resistance of Ni–Cr alloys is mainly endowed by the passivating oxides, e.g., Cr_2O_3 and NiO. Furthermore, the related metals and (hydr)oxides find other versatile applications in solid-oxide fuel cells, lithium-ion batteries, catalysis, biomedicine, and resistive logic devices[20,21]. The stability of these materials and devices under many working environments (e.g., humid air and aqueous solutions) will determine their performance and lifetime.

Elemental partitioning in bulk alloys found after certain thermal processing cycles is a ubiquitous phenomenon that can be exploited to tune physical properties; nonetheless, it may also bring some adverse effects on the corrosion resistance of alloys if uncontrolled. The composition bipartition of a Ni–Cr alloy ($x_{Cr} = 59$ at%) into the Ni-rich (γ-Ni phase) and Cr-rich (α-Cr phase) regions after both casting and annealing processes (Fig. 1a) has recently been clearly characterized and controlled by Miller et al.[22]. The correlation between (local) alloy composition and surface corrosion resistance is well exemplified by the electrochemical measurements by Xie et al.[23] on the anodic dissolution of Ni–Cr alloys (with 0–24 at% of Cr) in 0.1 M H_2SO_4 solution. Linear sweep voltammetry measurements show that the polarization current density decreases by two orders of magnitude when x_{Cr} reaches the critical value of 13 at% (Fig. 1b). This result has been explained with percolation theory[23,24], whereby upon selective dissolution of Ni, x_{Cr} approaches the two-dimensional percolation threshold above which a well-linked "-Cr–O- network" forms and then sharply improves the surface passivation. As further indicated by Fig. 1b, the corrosion resistance of Cr_2O_3 is superior to that of NiO because more Cr replacing Ni (i.e., more Cr_2O_3 to form on alloy surface) leads to the decreased current density (i.e., enhanced corrosion resistance). Duarte et al.[25] have also observed another kind of composition–corrosion correlation in the glass-forming $Fe_{50}Cr_{15}Mo_{14}C_{15}B_6$ steel (with a glass transition temperature at 550 °C), where Fe, Cr, and Mo are distributed homogeneously in the as-quenched amorphous sample (Fig. 1c), and a conformal Cr-based passivating film provides passivity in the 0.1 M H_2SO_4 solution (Fig. 1d). However, this amorphous steel has the onset first and second crystalization temperatures at 602 and 641 °C, respectively, thus as the annealing temperature increases from 550 up to 800 °C (for 20–60 min), the elemental partitioning driven by the favored formation of both Cr-rich $(Fe,Cr)_{23}(C,B)_6$ and Cr-depleted η-Fe_3Mo_3C phases gradually increases. The Cr-depleted areas then exhibit preferentially higher dissolution of Fe and Mo, largely activated by the formation of Cr-poor phases that begin at a

[1]Department of Materials Science and Engineering, Northwestern University, Evanston, IL 60208, USA. [2]Research Center for Advanced Interdisciplinary Sciences, Ningbo Institute of Materials Technology and Engineering, Chinese Academy of Sciences, Ningbo 315201, China. [3]Ira A. Fulton School of Engineering, Arizona State University, Tempe, AZ 85287, USA. ✉email: jrondinelli@northwestern.edu

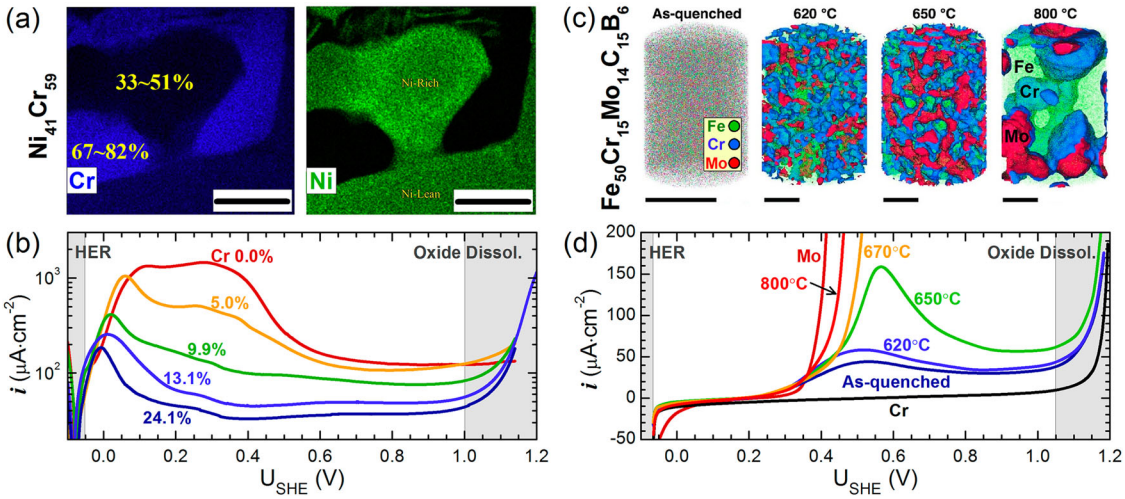

Fig. 1 Experimental characterizations of the thermodynamic and electrochemical behaviors of Ni–Cr alloys and Fe–Cr–Mo–C–B steel. **a**, **c** The characterization results by scanning electron microscopy plus energy dispersive X-ray spectroscopy (SEM-EDS) and atom probe tomography (APT) revealing the elemental partitionings in a Ni–Cr alloy (scale bar: 500 nm)[22] and a Fe–Cr–Mo–C–B steel (scale bar: 20 nm)[25]. **b**, **d** The composition dependence of polarization current density for Ni–Cr alloys[23] and annealing-temperature dependence of the polarization current density for Fe–Cr–Mo–C–B steel[25]. The electrochemical measurements in (**b**) and (**d**) are both carried out in 0.1 M H_2SO_4 solution (pH ≈ 0.88). Figures are adapted with permissions from Elsevier Limited[22], Springer Nature Limited[23], and the American Association for the Advancement of Science[25].

temperature of ~650 °C and continue for higher temperatures. This results in a sudden rise of polarization current density (Fig. 1d).

To guide the precise heat-treatment process toward superior corrosion resistance of Ni–Cr alloys, it is essential to establish an accurate understanding of the driving forces for the elemental partitioning in Ni–Cr alloys and their electrochemical behaviors. In recent decades, Ni–Cr alloys have been studied using both experiment and theory, however, an accurate quantitative understanding of their thermodynamic and electrochemical behaviors is still limited. For the thermodynamic stability of Ni–Cr alloys, their free energies of formation ($\Delta_f G$) were obtained in previous theoretical studies by fitting the experimentally determined phase boundaries[26–29]. To establish a deeper thermodynamic understanding, it is still desirable to accurately deterimine the individual contributions of different components (e.g., electronic energy, vibrational free energy, and configurational entropy) in those fitted $\Delta_f G$ values. Many first-principles calculations have also been carried out to reveal the thermodynamic properties of Ni–Cr alloys[30–35]. However, their systematic composition- and temperature-dependent $\Delta_f G$ values are still lacking and necessitate further high-fidelity calculations to facilitate precise understanding of many thermodynamic behaviors. Furthermore, an accurate electrochemical understanding of Ni–Cr alloys remains incomplete owing to the inaccuracy or even absence of the $\Delta_f G$ values for many oxidation and corrosion products[36,37], as discussed next. Obtaining accurate thermodynamic and electrochemical results is also a prerequisite for reliably analyzing the correlation between composition, heat treatment, and corrosion resistance for Ni–Cr alloys.

Pourbaix diagrams can be used to efficiently map the electrochemical stabilities of metals, oxides, and (oxy)hydroxides in terms of solution pH and electrode potential[36,38]. Such electrochemical stability can also be compared with atmospheric stability, which can help establish a comprehensive understanding of the interaction of alloys with their environments. The construction of a Pourbaix diagram requires the $\Delta_f G$ values of all the involved species (metal, compounds, and aqueous ions) as input. The $\Delta_f G$ values for many oxides and (oxy)hydroxides estimated in the experiment may turn out to be inaccurate due to many unavoidable technical and physical issues (e.g., defect contamination, mass loss, uncontrollable temperature, and reaction byproducts) associated with measurement techniques based on combustion and dissolution[20,36,37]. In various thermodynamic databases, the experimental $\Delta_f G$ values per formula unit (f.u.) for some important transition-metal oxides may exhibit large uncertainties (e.g., 0.5 eV per f.u. for NiO and 1.6 eV per f.u. for Co_3O_4), and the $\Delta_f G$ values for some are also unavailable (e.g., Cr_3O_4)[37]. It is these complexities that have led to the disagreement between some derived Pourbaix diagrams and various direct electrochemical characterizations[36,37]. Alternatively, first-principles calculations based on density-functional theory (DFT) can be used to solve this long-standing problem[36]. High-fidelity calculations using exact nonlocal exchange potentials can be used to obtain accurate $\Delta_f G$ values, from which reliable Pourbaix diagrams for transition-metal systems can be constructed and validated[36,37,39,40]. The first-principles Poubaix diagrams for transition metals have also been widely referred to by many recent electrochemical experiments in the fields of, e.g., corrosion[41–45], catalysis, and energy[46–54], where these diagrams guide the design and characterization of many related materials, and even have been applied to understand geological processes (rock weathering in acid rains) on both the ancient Earth and Mars[55,56].

Here we formulate an ab initio thermodynamic model, which includes the essential vibrational entropy of the alloy, to obtain the temperature- and composition-dependent $\Delta_f G$ values for Ni–Cr alloys. The thermodynamic results allow us to explain the experimentally observed elemental partitioning and phase transformations induced by different heat treatments. We show that DFT calculations using hybrid functionals are required to obtain accurate $\Delta_f G$ values for Ni- and Cr-based oxides, hydroxides, and oxyhydroxides, as well as their binary-metal oxides ($NiCr_2O_4$ and $NiCrO_4$), from which we further construct reliable Pourbaix diagrams for Ni–Cr alloys. After having individually established the highly accurate thermodynamic and electrochemical descriptions for Ni–Cr alloys, we then explain various experimental passivation and corrosion behaviors of related alloys, demonstrating a correlation between elemental partitioning and corrosion resistance, as well as the utility of the model. We conclude by describing how the thermodynamic and electrochemical mechanisms revealed from our study can rationalize the empirical design of various industrial Ni–Cr alloys.

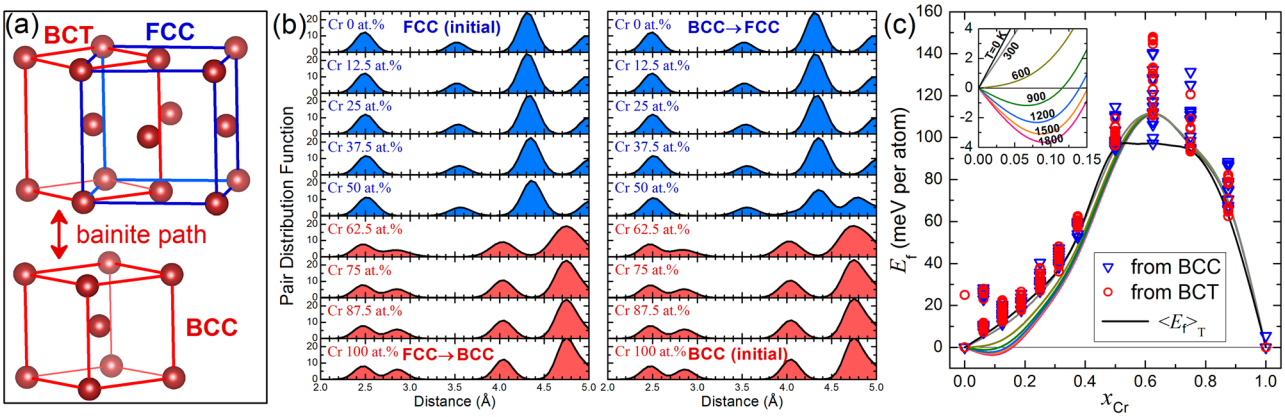

Fig. 2 The composition-dependent atomic structure and electronic energy of Ni–Cr alloys. a The bainite transformation path between FCC and BCC unit cells, **b** the pair distribution functions of the structures of Ni–Cr alloys calculated from the initial FCC (BCT) and BCC supercells, and **c** the calculated electronic energies of formation (E_f) and their thermal averages ($\langle E_f \rangle_T$).

RESULTS AND DISCUSSION

Structures and magnetism of $Ni_{1-x}Cr_x$

Elemental Ni exhibits ferromagnetism within a face-centered-cubic structure (FM-FCC), whereas elemental Cr exhibits antiferromagnetism within a body-centered-cubic structure (AFM-BCC). With increasing Cr content (x_{Cr}) in the $Ni_{1-x}Cr_x$ solid solution, the magnetism-structure configuration will continuously transform from FM-FCC to AFM-BCC, with the intermediate configurations having distorted atomic structures and disordered spins. To capture such transformations in our DFT calculations, we need to utilize a supercell model that can accommodate both the FCC and BCC structures. To that purpose, we use the bainite transformation path, which has been proposed as the preferred BCC-FCC transformation path for many transition metals (e.g., Ni–Cr alloys and steels)[30,31,57–60], to connect the BCC and FCC lattices (Fig. 2a) by using a tetragonal bainite strain[61] given as

$$\varepsilon_B = \begin{pmatrix} \epsilon & 0 & 0 \\ 0 & \epsilon & 0 \\ 0 & 0 & -\frac{\epsilon(\epsilon+2)}{(1+\epsilon)^2} \end{pmatrix}, \quad (1)$$

where the parameter ϵ equals 0 and −0.109 at the BCC and FCC ends of the path, respectively, and the FCC lattice derived from the BCC one is expressed by the body-centered-tetragonal (BCT) cell (see Fig. 2a). To construct the initial atomic structures of the $Ni_{1-x}Cr_x$ solid solutions for our DFT calculations, we first generate a sufficiently large BCC supercell (4 × 4 × 4, 128 atoms) to accommodate the randomly placed Ni and Cr solutes. Then, we use the bainite strain to transform the BCC supercell into a BCT one, as plotted in Fig. 2a and Supplementary Fig. 1. This use of the bainite path is an effective structural modeling approach, because the FCC (BCT) and BCC lattices are treated equally as the initial structures at any solid-solution composition, and the spontaneous supercell distortions occurring during their DFT optimizations can help us obtain a sufficiently large ensemble of random lattice distortions in an unbiased way. The pair distribution functions of all the optimized structures (Fig. 2b) clearly show that both initial FCC and BCC supercells can lead to the correct alloy-structure variation and a common structural transition at $x_{Cr} \sim 62.5$ at%. Such structural transition is also simultaneously reflected by the calculated electronic energies of formation (E_f) of $Ni_{1-x}Cr_x$ (Fig. 2c), which further validates our structural modeling approach. In addition, the E_f values of $Ni_{1-x}Cr_x$ calculated using the 2 × 2 × 2, 3 × 3 × 3, and 4 × 4 × 4 supercells are compared in Supplementary Fig. 2, where the converged composition-dependent profile validates the high accuracy of a 4 × 4 × 4 supercell.

For each composition in a specific initial configuration (BCC or BCT), we generate six random solute distributions in the supercell to mimic the realistic $Ni_{1-x}Cr_x$ solid solution. We also set FM and two AFM states as the initial magnetic configurations. In one AFM state, Ni atoms have the spin polarization reverse to that of the Cr atoms, and in another AFM state, the two inequivalent sites of the BCC lattice have the reverse spin polarizations. Therefore, for each composition sampled in the $Ni_{1-x}Cr_x$ space, we create 36 random magnetism-structure configurations to treat the magnetic disorder and structural distortions. When comparing the E_f values based on the random-supercell model here to the previous results based on a cluster-expansion (CE) model (in small BCC/FCC supercells ≤16 atoms, see Supplementary Fig. 2)[62], it is clear that the CE E_f values exhibit larger energetic scattering than those obtained by our approach. This may be due to the difficulty of the CE model in treating the mutually coupled disordered magnetism and distorted lattices in solid solution $Ni_{1-x}Cr_x$. Note that we focus exclusively on the solid-solution phase because it is the most relevant phase in experimental samples; the possible precipitation of ordered Ni_2Cr is omitted from further consideration because of its minor chemical role and debatable stability[22].

Free energies of formation for alloys and compounds

The $\Delta_f G$ of a $Ni_{1-x}Cr_x$ alloy is defined as the free-energy change associated with the mixing of elemental Ni and Cr into a random alloy, as expressed by

$$\Delta_f G = E_f + \Delta\tilde{F}_e + \Delta F_{vib} - TS_c, \quad (2)$$

where the electronic energy of formation E_f is derived using the electronic energies obtained from DFT calculations; $\Delta\tilde{F}_e$ is the contribution from electronic excitations at a finite temperature[63–65]; ΔF_{vib} is the vibrational free energy contribution as calculated using a Debye model designed below; S_c is the configurational entropy for the atomic distribution in a solid solution and brings an energetic contribution of $-TS_c$ ($= k_B T \sum_i x_i \cdot \ln x_i$, i = Ni and Cr)[66]. To better model the realistic $Ni_{1-x}Cr_x$ solid solutions with fully random magnetism-structure configurations, E_f here is replaced by its thermal average $\langle E_f \rangle_T$ (see Supplementary Fig. 3 for more details) over all the 36 considered magnetism-structure configurations at each composition. The calculated temperature-dependent $\langle E_f \rangle_T$–x_{Cr} curves are shown in Fig. 2c.

For a solid compound $Ni_{m_1}Cr_{m_2}O_{n_1}H_{n_2}$, its standard $\Delta_f G$ is expressed by[37]

$$\Delta_f G = E_f + \Delta\tilde{F}_e + \Delta F_{ph} - \frac{n_1}{2} g_0(O_2) - \frac{n_2}{2} g_0(H_2), \quad (3)$$

where the elemental metals and standard molecular gases (i.e., O_2 and H_2, 1 bar) are the reference systems; ΔF_{ph} is the contribution of vibrational free energy derived from phonon spectra; g_0 is the free-energy change of a reference gas from 0 K to the targeted temperature as measured by experiment[67]. The relevant compounds include many mono-metal oxides (NiO, NiO_2, Cr_2O_3, and CrO_2) and (oxy)hydroxides ($Ni(OH)_2$, NiOOH, and CrOOH), as well as two binary-metal oxides ($NiCr_2O_4$ and $NiCrO_4$).

In the calculations of alloy $\Delta_f G$ values by Eq. (2), the F_{vib} values of Ni–Cr alloys and elemental metals (Ni and Cr) are derived by using an efficient Debye model designed here (see the next section). It is practically unfeasible to carry out computationally expensive phonon calculations for the large $4\times4\times4$ alloy supercells. However, the phonon spectra are calculated to derive the compound $\Delta_f G$ values by Eq. (3). The accuracy of the Debye model will be clearly validated (in the following two sections) by the comprehensive theory-experiment comparisons on Debye temperature, $\Delta_f G$ values, x–T phase diagram, and elemental segregation behaviors for Ni–Cr alloys. In addition, the F_{vib} values for elemental metals derived from both the Debye model and phonon spectra are further compared in the Supplementary Information (see Supplementary Fig. 5), which also indicates a very small energetic deviation (8–19 meV) at regular heat treatment temperatures (600–1500 K). Furthermore, the effects of thermal expansion and magnetic thermal excitations are both neglected in the alloy and compound $\Delta_f G$ values because their calculations will demand complicated and expensive first-principles procedures[64,68–70]. Such simplifying treatment can largely upgrade the efficiency of ab initio thermodynamic and electrochemical calculations here, with the numerical accuracy for alloy and compound $\Delta_f G$ values being safely guaranteed, which has also been discussed in detail in the Supplementary Information (Section C). The allowability of such simplification for a $\Delta_f G$ expression benefits from the cancellation between the thermal-expansion (and magnetic-excitation) effects in an alloy/compound and its reference elements (by Eqs. (2) and (3)).

The theoretical method to construct a Pourbaix diagram using these $\Delta_f G$ values as input is described in detail in the Supplementary Information (Section I). Summarily, the relative chemical potentials of all the involved species are calculated based on the reaction paths connecting them, and a Pourbaix diagram can be obtained when all the most stable species at different electrochemical phase spaces (in terms of solution pH value and electrode potential) are determined[36,37].

Debye model designed for $Ni_{1-x}Cr_x$

It is computationally challenging to calculate the F_{vib} (in Eq. (2)) for a large alloy supercell with random magnetic solutes. The combination of DFT and a Debye model provides an efficient option that has been widely used to study various metals, including Ni, Ti, Fe, and Ni_3Al[71–75]. In the Debye model, F_{vib} is expressed in terms of a Debye temperature (Θ_D), i.e., $F_{vib} = k_B T\left[\frac{9}{8}\beta + 3\ln(1-e^{-\beta}) - D(\beta)\right]$, where β equals Θ_D/T, and $D(\beta)$ is the Debye integral expressed by $D(\beta) = \frac{3}{\beta^3}\int_0^\beta x^3/(e^x-1)dx$ (see the Supplementary Fig. 4). The accuracy of a Debye model is largely determined by the value of Θ_D, which is expressed as

$$\Theta_D = f(v)\cdot\frac{\hbar}{k_B}\left(6\pi^2 V^{\frac{1}{2}}\right)^{\frac{1}{3}}\cdot\sqrt{\frac{B}{m}}, \tag{4}$$

where V and m are the volume and mass per atom, respectively; v and B are the Poisson's ratio and bulk modulus, respectively. The v in the Voigt–Reuss–Hill (VRH) approximation for polycrystalline alloys can be used to derive the coefficient $f(v)$[72,76] as

$$f(v) = \left\{3\left[2\left(\frac{2}{3}\frac{1+v}{1-2v}\right)^{3/2} + \left(\frac{1}{3}\frac{1+v}{1-v}\right)^{3/2}\right]^{-1}\right\}^{1/3}. \tag{5}$$

To further simplify the Debye model, Moruzzi et al. have used an approximated constant of 0.617 for the coefficient $f(v)$ [71]. We denote these two Debye models as the *VRH model* and *Moruzzi model*, respectively.

We approximate the alloy volume and bulk modulus in Eq. (4) by their equilibrium values (V_0 and B_0), which can bring additional computational convenience while maintaining accuracy, as shown in the following. The B_0 values are derived from the equation of states (EOS) calculated by DFT, and the results for $Ni_{1-x}Cr_x$ structures optimized from both the initial BCC and BCT supercells are shown in Fig. 3a. The average of these two groups of B_0 values is used to derive the Θ_D at each composition. The computational challenge to obtain a well-defined EOS here is clearly shown by the inset in Fig. 3a, where the disordered and itinerant magnetism, as well as its strong coupling with the lattice, gives a large scatter to the energies. To reduce the large variance, we examine many different initial magnetic configurations and volumes. We then perform a high-quality EOS fitting after obtaining a sufficient number of electronic energies (in solid circles) exactly residing on the convex-hull line. From both Fig. 3a and Fig. 2c, we find that the average B_0 has a chemical trend that generally reverses to that of E_f, i.e., the stiffness of solid-solution $Ni_{1-x}Cr_x$ tends to decrease

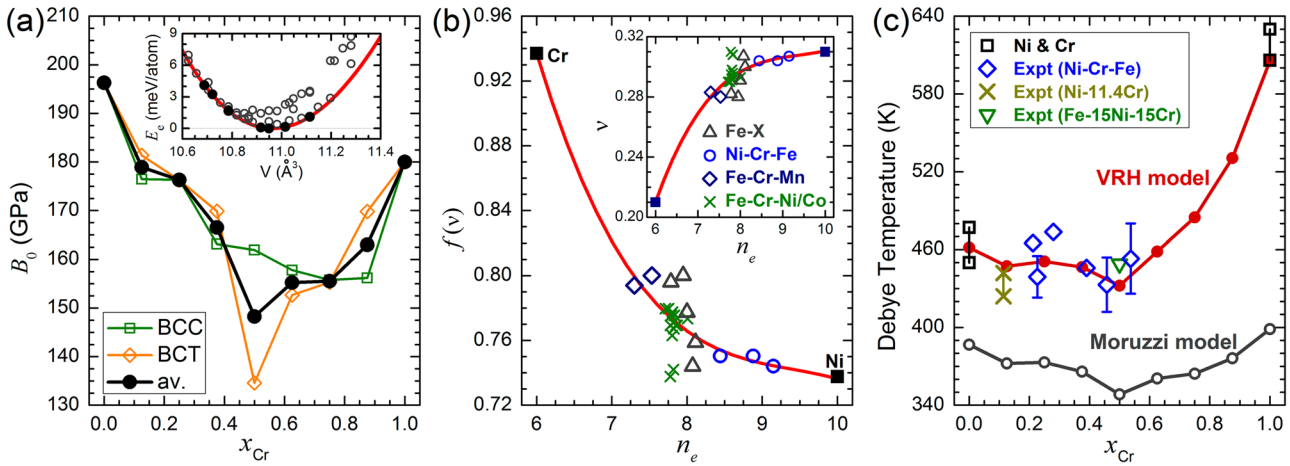

Fig. 3 The calculated parameters for the designed Debye model. a The calculated bulk moduli (B_0) using equilibrium alloy volumes and (inset) an example of EOS fitting for $Ni_{1-x}Cr_x$ with $x_{Cr} = 12.5$ at%. **b** The f–n_e curve derived from the v–n_e curve (inset) that is fitted based on the experimental data for Ni, Cr, Ni–Cr–Fe, Fe–Ni/Cr/Co/Mn, and Fe–Cr–Mn/Co/Ni[78–85]. **c** The calculated Debye temperatures (Θ_D) from the VRH and Moruzzi models, compared with experimental data for Ni, Cr, Ni–Cr, Ni–Cr–Fe–(Mo/Cu/Mn), and Fe–Ni–Cr[79,80,86–88].

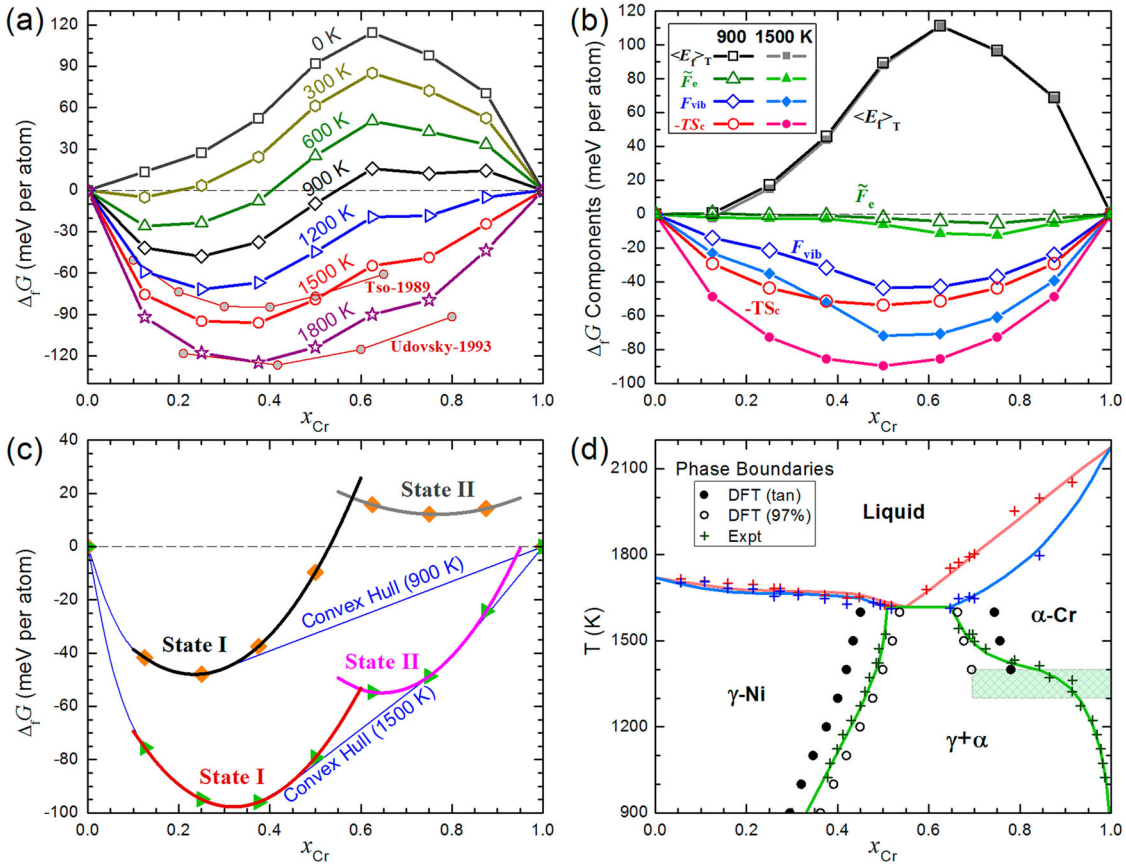

Fig. 4 The composition-dependent thermodynamic energies and phase diagram of Ni–Cr alloys. a The free energies of formation ($\Delta_f G$) of Ni–Cr alloys with experimental data[26,27] at 1500 K provided for comparison. **b** The $\Delta_f G$ components at 900 K and 1500 K, and **c** the two equilibrium states at 900 K and 1500 K. **d** The DFT simulated Ni–Cr composition-temperature phase diagram with the two-phase boundaries calculated here compared to the corresponding two experimental boundaries[27].

with increasing its E_f (decreasing its phase stability). This behavior reflects a generic relationship between alloy stiffness and phase stability, which has also been observed by Maisel et al. in Ni–Ta/W/Al and Cu–Al alloys[77].

Usually, elastic constants can be obtained by fitting the corresponding energy-strain relationships[61], and then be used to derive v and $f(v)$. However, as the inset in Fig. 3a shows, large energetic scattering occurs with variable strain owing to the irregular changes of disordered spins. This makes it computationally challenging to obtain a well-defined energy-strain relationship. Rather than using this approach, we collect the reported experimental v values for various Ni–Cr and Fe-based alloys (Ni–Cr, Ni–Cr–Fe, Fe–Ni/Cr/Co/Mn, and Fe–Cr–Mn/Co/Ni) that have similar lattice structures and electronic structures[78–85], and then fit the variation of v with respect to the number of valence electrons (n_e), as shown in the inset to Fig. 3b, to obtain an accurate $f(v)$. We then use this v–n_e relationship to derive the f–n_e curve (by Eq. (5)), which, as we show describes well the chemical trend in the experimental f values for elemental metals (Ni and Cr) and the Ni–Cr, Fe–Ni, and Fe–Cr alloys (Fig. 3b). The average B_0 values and f coefficients obtained are then finally used to compute the Θ_D–x_{Cr} relationships for both VRH and Moruzzi models. From Fig. 3c, we find that the VRH Θ_D–x_{Cr} curve accurately agrees with many reported experimental data for Ni–Cr, Ni–Cr–Fe, and Fe–Ni–Cr alloys[79,80,86–88]. However, the Moruzzi model underestimates Θ_D by 70–210 K because $f = 0.617$ is lower than the actual values ($0.73 \le f \le 0.94$). The comparison between VRH and Moruzzi Θ_D values (Fig. 3c) can help us quantitatively understand the importance of composition dependence in both B_0 and f for the accurate prediction of Θ_D.

Thermodynamic stability of $Ni_{1-x}Cr_x$

We now use the accurate Θ_D values from the VRH model and Eq. (2) to calculate the composition- and temperature-dependent $\Delta_f G$ values of the $Ni_{1-x}Cr_x$ solid solutions (Fig. 4a). We further decompose the individual energetic contributions from the electronic energy of formation ($\langle E_f \rangle_T$), electronic excitations ($\tilde{F}_e$), atomic vibrations (F_{vib}), and configurational entropy ($-TS_c$) at two representative temperatures (900 K and 1500 K, Fig. 4b). Decompositions of $\Delta_f G$ at other temperatures are shown in the Supplementary Fig. 6. We find that the $\Delta_f G$ values are all positive at temperatures of $\lesssim$200 K, and the positive $\langle E_f \rangle_T$ plays the deterministic role in the unfavored thermodynamic stability of Ni–Cr solid solutions at very low temperatures. Temperatures $\gtrsim$600 K are more relevant for metallurgical processing; here, we find that the $\Delta_f G$ curve shifts monotonically to lower energy upon heating (Fig. 4a), mainly due to the negative energetic contributions from configurational and vibrational entropies (Fig. 4b). The low-x_{Cr} part of the $\Delta_f G$ curve ($x_{Cr} \sim 10$ at%) firstly becomes negative at temperatures of $\gtrsim$200 K, and the high-x_{Cr} part ($x_{Cr} \sim 75$ at%) only becomes negative at temperatures of $\gtrsim$1000 K.

Two groups of experimental $\Delta_f G$ values at 1500 K are also provided in Fig. 4a, which are converted from the original data at 1550 K and 1423 K[26,27], respectively, using the $\Delta_f G$–T relationship established here (see the Supplementary Fig. 7 and Supplementary Table 1 for details). Although the same phase transformation measurements have been referred to for the analytical fittings, these two groups of experimental $\Delta_f G$ data have a difference of 40–50 meV per atom. Our first-principles $\Delta_f G$ values at 1500 K reside well between these two groups of $\Delta_f G$ values at $x_{Cr} \lesssim 40$ at%,

above which the elemental partitioning tends to be triggered in $Ni_{1-x}Cr_x$ and influences the accuracy of previously fitted energies. Furthermore, we can readily identify two equilibrium states from the first-principles $\Delta_f G$ curves. We analyze these two equilibrium states at different temperatures by fitting the $\Delta_f G$ data using parabolic curves, for which the fitted curves and corresponding convex hulls at 900 K and 1500 K are shown in Fig. 4c (see Supplementary Figs. 8 and 9 for more fitting and analysis results). We denote the major state at a lower x_{Cr} ($\lesssim$40 at%) as *State I*, and the second state at a higher x_{Cr} (65–80 at%) as *State II*. The equilibrium $\Delta_f G$ of State I becomes negative at temperatures $\gtrsim$ 200 K, and its equilibrium x_{Cr} increases from 0 to 36 at.% with increasing temperature from 200 to 1800 K (see Supplementary Fig. 9 for more details). The equilibrium $\Delta_f G$ of State II only becomes negative at high enough temperatures of $\gtrsim$1000 K, and its equilibrium x_{Cr} decreases from 72 at% down to 64 at% with increasing temperature from 1000 to 1800 K (see Supplementary Fig. 9).

At high temperatures (e.g., 1500 K in Fig. 4c), the parabolic curves of both equilibrium states have tangential contacts with the convex-hull curve. In the compositional range between these two contact points, the combination of States I and II as a two-phase system have a lower $\Delta_f G$ than that of either single phase defined by State I or II. At temperatures of $\lesssim$1330 K, the convex-hull curve only has a tangential contact with the parabolic curve of State I (Fig. 4c and Supplementary Fig. 8), i.e., State II becomes metastable below this critical temperature. If the two tangential contacts are used to define the I/I + II and I + II/II phase boundaries and are plotted in the x_{Cr}–T phase diagram for Ni–Cr alloys (Fig. 4d, solid circles) together with the experimental measurement results[26,27], we can find that States I and II correspond to the Ni-rich γ and Cr-rich α phases, respectively. In addition, a phase transformation in the experiment may be practically viewed as complete when a phase ratio (r_p) of 97–99% is achieved, like the situation in the well-known measurement of continuous cooling transformation curves (or called time-temperature transformation curves) for alloys. This can be used to set a possible energetic uncertainty for tangential contacts ($\delta G = -k_B T \cdot \ln r_p$), which will make the I/I + II (I + II/II) phase boundary heightened (lowered) by 6–8 at% at $r_p = 97\%$. From Fig. 4d, it can be clearly seen that the $\gamma/\gamma + \alpha$ and $\gamma + \alpha/\alpha$ boundaries measured in the experiment reside between the two groups of DFT results at r_p values of 97% and 100%. The metastability of State II at <1330 K revealed in our DFT calculations also agrees with the divergent experimental $\gamma + \alpha/\alpha$ boundary at temperatures of <1400 K.

The elemental-partitioning tendency in Ni–Cr alloys and the underlying driving force can be quantitatively understood when the composition- and temperature-dependent $\Delta_f G$ values (Fig. 4a–c) and the phase diagram (Fig. 4d) are jointly used for the thermodynamic analysis. The elemental partitionings in Ni-59 at% Cr after different heat treatments, as observed by Miller et al.[22] (Fig. 1a), provide good use cases to demonstrate the capability and accuracy of our first-principles-based thermodynamic results. After the homogenization process at the melting state ($T \gtrsim$ 1700 K), an elemental-partitioning process already appears in the as-cast Ni–Cr sample, which should be attributed to the unavoidable local bipartition of Ni-59 at%Cr into States I and II during the fast cooling step. As characterized by scanning electron microscopy and energy dispersive spectroscopy (SEM-EDS), the resultant Cr-depleted region is found to have an x_{Cr} of 48–55 at% and is a little higher than the x_{Cr} of the I + II/II boundary at 1700 K (44–52 at%, Fig. 4d). Thus, the elemental partitioning of this Cr-depleted region towards an equilibrium I + II ($\gamma + \alpha$) state will be further activated during any cooling process or annealing process at temperatures < 1700 K. This result explains well the observed precipitation of narrow-stripe α phase within the interdentritic γ phase during the annealing process at 1173 K for 4 h. The Cr-rich region has a x_{Cr} of 67–72 at%, which is also very close to the equilibrium x_{Cr} (65–72 at%) of State II within the temperature range of 1000–1700 K. Based on the metastability of State II at temperatures of $\lesssim$1330 K, this Cr-rich region will tend to further separate into State I plus pure Cr, which also explains the appearance of very high x_{Cr} ($\gtrsim$80 at%) at the α/γ interfaces after a long-period (1000 h) annealing at 773 K. Furthermore, according to the relationship between $\Delta_f G$ and convex-hull curves at $T \gtrsim$ 1400 K (Fig. 4c and the Supplementary Fig. 8), a narrow region appears with coexisting State II and pure Cr. However, the energetic fluctuations caused by structural distortions and spins might be large enough (~10 meV per atom) to remove this weak phase bipartition tendency.

Our thermodynamic stability analysis of $Ni_{1-x}Cr_x$ provides a general and quantitative understanding for the compositions and heat treatments used by many industrial grade Ni–Cr alloys, e.g., the Inconel series, Incoloy series, Nimonic series, Udimet R41, Incotherm TD, and Waspaloy. Supplementary Table 2 shows that their x_{Cr} values reside between 14.3 and 33.5 at% and their heat-treatment temperatures for solid-solution homogenization (precipitation hardening, grain growth, and stress release) are at 1200–1500 K (900–1200 K). If we ignore the chemical complexity brought by other elements (e.g., Fe, Mo, Co, Ti, Al, and C) in these industrial Ni–Cr alloys, we find that their x_{Cr} range coincides with the equilibrium x_{Cr} of State I at 600–1600 K (see Fig. 4a and the Supplementary Figs. 8 and 9). Therefore, equilibrium State I has always been closely approached during the fabrication of these industrial alloys. This can guarantee the highest stability (the lowest $\Delta_f G$) for a Ni–Cr solid solution and then allow its grain growth, second-phase precipitation, mechanical properties, and corrosion/oxidation resistance to be tuned by other alloying elements without destroying the framework lattice. It is also understandable that the heat-treatment temperatures (900–1500 K) used in industry are intermediate within the theoretical range (600–1600 K), because a too-low temperature limits the microstructural evolutions (e.g., grain growth and precipitation) during an industrial processing time (from minutes to 24 h), and a too high temperature makes the microstructure kinetically over excited and unfavored for meticulous tuning. In thermal barrier coatings for gas turbines, the optimized compositions for bond-coat NiCrAlY and NiCrCoAlY (x_{Cr} = 16–22 at%)[4,89–93] should also comply with such thermodynamic principles.

Stability of passivating oxides

The oxidation and dissolution trends of Ni–Cr alloys in electrochemical conditions are largely determined by the stability of native passivating oxides (e.g., NiO, Cr_2O_3, and $NiCr_2O_4$) formed on the alloy surfaces. To reliably understand and predict their electrochemical stability, accurate standard free energies of formation ($\Delta_f G^0$) at room temperature for many candidate solid compounds (oxides, hydroxides, and oxyhydroxides) involved in passivation are required to construct ambient Pourbaix diagrams[36]. Figure 5a shows our calculated $\Delta_f G^0(T)$ curves for the two most important mono-metal oxides (NiO and Cr_2O_3) and two binary-metal oxides ($NiCr_2O_4$ and $NiCrO_4$). The calculated $\Delta_f G^0$s at 298.15 K for all considered solid compounds, together with the standard chemical potentials of participating aqueous ions collected from experimental databases[38,94] are listed in Supplementary Table 3. The thermal contribution to $\Delta_f G^0$ (see Eq. (3)) mainly comes from both the vibrational free energy of the solid compound (ΔF_{ph}) and the free-energy changes of reference gases (g_0). The calculated phonon spectra and vibrational free energies of all those solid compounds and elemental Ni and Cr are shown in Supplementary Fig. 10, and the g_0 values for standard O_2 and H_2 gases (−0.54 and −0.32 eV at 298.15 K) are from the experimental databases[67].

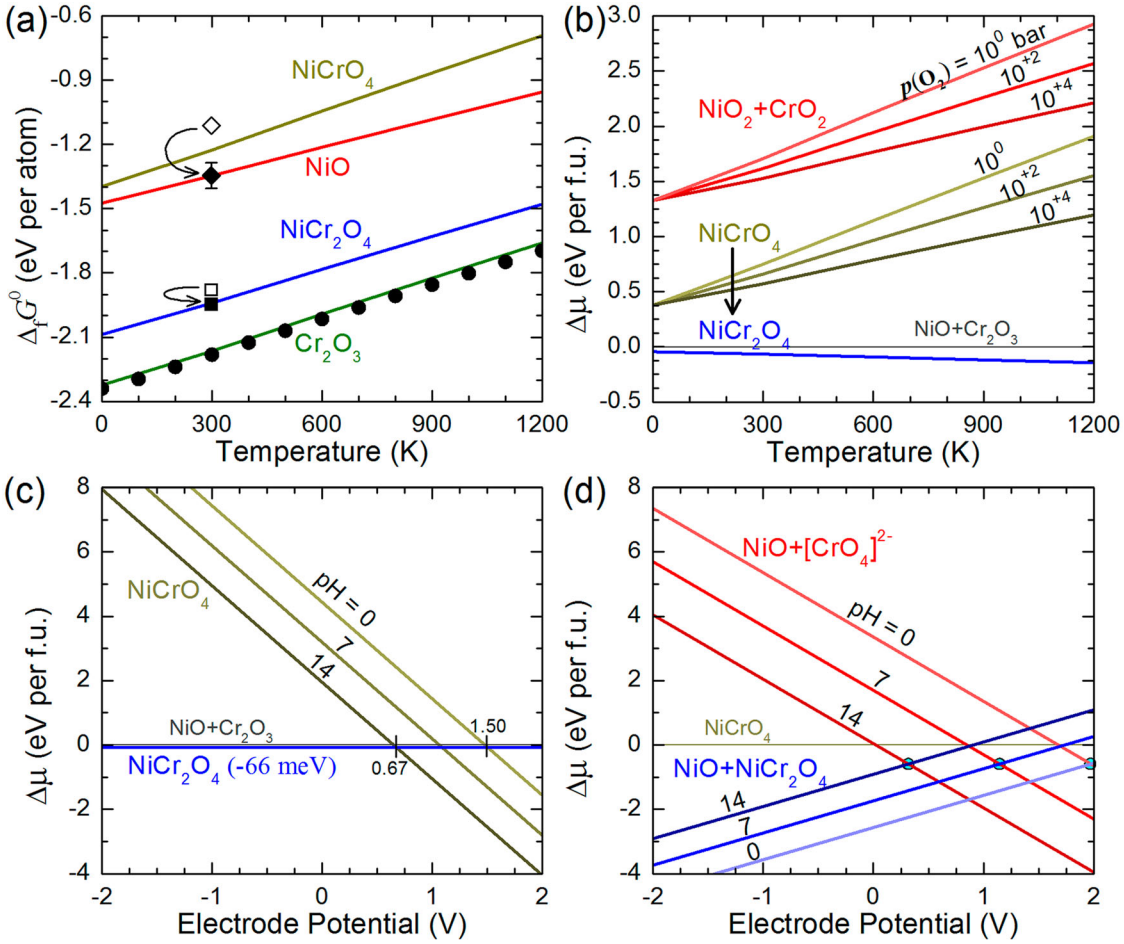

Fig. 5 The thermodynamic and electrochemical stabilities of different oxides. a The calculated standard free energies of formation (Δ_fG^0, normalized by the total number of atoms) for Cr_2O_3, NiO, $NiCr_2O_4$, and $NiCrO_4$ compared to available experimental data for Cr_2O_3 (from 0 to 1200 K, filled circles), NiO (at 298.15 K, empty diamonds), $NiCr_2O_4$ (at 298.15 K, empty squares), as well as the corrected experimental data for NiO and $NiCr_2O_4$ (filled diamonds and squares). **b** The relative chemical potentials ($\Delta\mu$) of $NiCr_2O_4$, $NiCrO_4$, and NiO_2+CrO_2 with respect to $NiO + Cr_2O_3$ at different atmospheric pressures and temperatures. The electrochemical $\Delta\mu$ values for **c** $NiCr_2O_4$ and $NiCrO_4$ with respect to $NiO + Cr_2O_3$, as well as for **d** $NiO + NiCr_2O_4$ and $NiO + [CrO_4]^{2-}$ with respect to $NiCrO_4$.

From Fig. 5a, it can be seen that the calculated $\Delta_fG^0(T)$ curve for Cr_2O_3 closely agrees with the experimental data[67]. The experimental Δ_fG^0s for both NiO and $NiCr_2O_4$ are only available at 298.15 K[38,94,95], and the latter is determined from the chemical potential of reaction ($\Delta\mu$) for the reaction of $NiO + Cr_2O_3 \rightarrow NiCr_2O_4$, plus the Δ_fG^0s for the reactants of NiO and Cr_2O_3[67]. Our recent DFT calculations and experimental characterizations have proved the underestimation of conventional experimental Δ_fG^0 for NiO (≈−1.11 eV per atom)[39,40], which has been corrected to be −1.35 eV per atom. Thus, the conventional Δ_fG^0 value for $NiCr_2O_4$ (−1.87 eV per atom) should be corrected to be −1.94 eV per atom. These corrected Δ_fG^0s for NiO and $NiCr_2O_4$ at 298.15 K then fall on the calculated $\Delta_fG^0(T)$ curves, as indicated by the arrows in Fig. 5a.

To further understand the relative stability of $NiCr_2O_4$ and $NiCrO_4$, we next use NiO and Cr_2O_3 as the reference oxides to derive the $\Delta\mu$ values of $NiCr_2O_4$ and $NiCrO_4$, which are also compared with the $\Delta\mu$ for $NiO_2 + CrO_2$ (phase coexistence) in Fig. 5b. The $\Delta\mu$ values for $NiCrO_4$ and $NiO_2 + CrO_2$ also depend on the pressure of O_2 gas owing to the higher oxidation degrees of cations therein with respect to those in $NiO+Cr_2O_3$, and we consider the range of $10^0 \le p(O_2) \le 10^4$ bar here. The negative $\Delta\mu(NiCr_2O_4)$ indicates the tendency of spontaneous formation of this spinel oxide through the chemical mixing of the mono-metal components, i.e., NiO and Cr_2O_3. The $\Delta\mu(NiCrO_4)$ is lower than $\Delta\mu(NiO_2 + CrO_2)$, which also indicates the tendency of spontaneous chemical mixing of NiO_2 and CrO_2. However, the $\Delta\mu(NiCrO_4)$ is higher than $\Delta\mu(NiCr_2O_4)$, showing the metastability of $NiCrO_4$. This well explains the experimental observations that although $NiCrO_4$ frequently appears under synthesis conditions with high temperatures (720–1120 K) and high oxygen pressures (2–3500 bar), it always finally transforms into $NiCr_2O_4$[96,97]. Because the cations in $NiCrO_4$ have higher oxidation degrees than those in $NiCr_2O_4$ (or $NiO + Cr_2O_3$), it may be possible to stabilize $NiCrO_4$ using a high enough electrode potential U (with respect to the standard hydrogen electrode, SHE) in an electrochemical system. The feasibility can be evaluated by calculating the variations of some relative $\Delta\mu$ values with respect to U (Fig. 5c, d). We find that although $NiCrO_4$ becomes more stable than $NiCr_2O_4$ when U reaches 1.50–0.67 V at pH values ranging from 0 to 14 (Fig. 5c), it never becomes the most stable electrochemical phase because other phases (e.g., $NiO + NiCr_2O_4$ and $NiO + [CrO_4]^{2-}$) always have lower $\Delta\mu$ values at any U (Fig. 5d).

Passivation of $Ni_{1-x}Cr_x$

In order to clearly map the trends of Ni–Cr alloys towards electrochemical oxidation and corrosion, we construct their Pourbaix diagrams (see Section I in Supplementary Information for theoretical details), and then separate the components by

cation-anion pairs into five subdiagrams (Fig. 6) for a clearer representation. In Fig. 6a–d, the phase domains of NiO, $Ni(OH)_2$, Cr_2O_3, and CrOOH are shown, respectively. We exclude the stable NiO and CrOOH phases when calculating the metastable domains of $Ni(OH)_2$ and Cr_2O_3, respectively. The phase domain of spinel $NiCr_2O_4$ in panel (e) is labeled by its boundary line (in dark blue) in panels (a–d). As pointed out above, the $Ni_{1-x}Cr_x$ solid solutions at $x_{Cr} \lesssim 34$ at% have the most favored thermodynamic stability for the fabrication of industrial Ni–Cr alloys, and Cr can be fully consumed by the reaction with Ni toward $NiCr_2O_4$ for alloy compositions with $x_{Cr} \lesssim 67$ at%. Thus, we explicitly show the phase domain of $NiCr_2O_4$ in the Cr Pourbaix diagram (Fig. 6e) to clearly present the formation condition of the spinel phase at the expense of Cr_2O_3. We consider a moderate aqueous-ion concentration ($[I]$) at 10^{-4} M because when the corrosive dissolution is active, the resultant $[I]$ will be relatively high ($\gtrsim 10^{-4}$ M). The left-side phase boundaries of the oxides and (oxy)hydroxides will shift to more acidic pH values, e.g., by pH ≈ 1 when $[I]$ is further increased to 10^{-2} M, owing to the lower stability for an aqueous ion at a higher concentration ($\mu = \mu^0 + k_B T \ln[I]$)[36].

It should be noted that compared to the $\Delta\mu$ values for metal oxidations, the $\Delta_f G$ values of Ni–Cr alloys at room temperature (0.0–0.08 eV per atom, Fig. 4a), especially those $\Delta_f G$ values at the optimal x_{Cr} of $\lesssim$34 at% (0.0–0.02 eV per atom), actually are negligibly small. Therefore, the composition dependence of alloy $\Delta_f G$ can be safely omitted in calculating the $\Delta\mu$ values for oxidation and corrosion reactions, and the alloy composition takes effect on the oxidation and corrosion trends through other mechanisms, e.g., the elemental partitioning process and the formation of passivating films, which can be effectively described by the calculated thermodynamic/electrochemical energies and phase diagrams here. The corrosion resistance of alloys, in part, relies on the passivating capabilities of native oxide films spontaneously grown on their surfaces because it is the passivating oxides that impart the reduced chemical reactivity and slow defect/mass transport to the alloy surfaces[40]. NiO and Cr_2O_3 are among the most important native passivating oxides for Ni–Cr alloys[3,5,39,98–102]. The large phase domains of NiO and Cr_2O_3 in the Ni–O and Cr–O diagrams (Fig. 6a, c) also clearly indicate their high electrochemical stability. The overlapping portion between the NiO and Cr_2O_3 domains tends to be replaced by the more stable $NiCr_2O_4$ (Fig. 6e).

According to the lower-potential boundaries for the NiO and Cr_2O_3 domains, the electrode potential for the oxidation of Cr in $Ni_{1-x}Cr_x$ is lower than that of Ni by 0.4 V, which will be considerably larger (0.9 V) if the inaccurate experimental $\Delta_f G$ for NiO is used in the electrochemical calculations. Then, during the spontaneous electrochemical formation of Cr_2O_3 on $Ni_{1-x}Cr_x$, the electrons released from the Cr → Cr_2O_3 transformation may render the alloy surface with a low-enough equilibrium electrode potential that can make the Ni element immune to oxidation. This will lead to a dealloying process on $Ni_{1-x}Cr_x$, with the Ni content being increased beneath the Cr_2O_3 film, and then the metal Ni turns to be oxidized into NiO after the depletion of Cr. The spontaneous Ni → NiO transformation has a higher (by 0.4 V) equilibrium potential and the surface potential will have an upshift upon the initiation of NiO formation. This electrochemical-oxidation sequence deduced from the Pourbaix diagrams of $Ni_{1-x}Cr_x$ well explains an important layered morphology comprising Cr_2O_3/NiO/alloy ubiquitously observed on Ni–Cr alloys after electrochemical treatments[5], as well as a similar morphology on Fe–Cr–Ni alloys (Ni-based oxide on top of Cr-based oxide)[103–106]. The selective formation of Cr_2O_3 as the top oxide layer is beneficial to the corrosion resistance because the mass transport should be reduced in the corundum Cr_2O_3 structure compared to the rock-salt NiO structure[1,3,107,108]. When a high enough exterior potential (e.g., 0.42 V) is imposed on the alloy surface to make the kinetically faster formation of NiO be electrochemically allowed, the formation of NiO layer above Cr_2O_3 can be observed on Ni–Cr alloys[41]. Similar NiO/Cr_2O_3/alloy morphology can also be observed on Ni–Cr and Ni–Cr–Fe alloys by oxygenating the solution[102], where oxygen reduction reaction[109,110] should have been stimulated, and the continuous electronic consumption will make the electrode potential sustained at a high level.

In many surface oxidation experiments under atmospheric conditions[98,100,101,111,112], a NiO layer often forms faster than Cr_2O_3 due to the higher growth kinetics of NiO. Then the more thermodynamically favored Cr_2O_3 (Fig. 5a) will nucleate at some defective sites (e.g., grain boundaries), leading to a flat NiO layer with Cr_2O_3 nodules interspersed therein. According to the higher thermodynamic stability of $NiCr_2O_4$ than NiO + Cr_2O_3 (Fig. 5b), we can deduce that $NiCr_2O_4$ tends to form at the existing Cr_2O_3/NiO and Cr_2O_3/Ni interfaces, which is in good agreement with the experimental observations[98,113]. The kinetic mechanisms at the

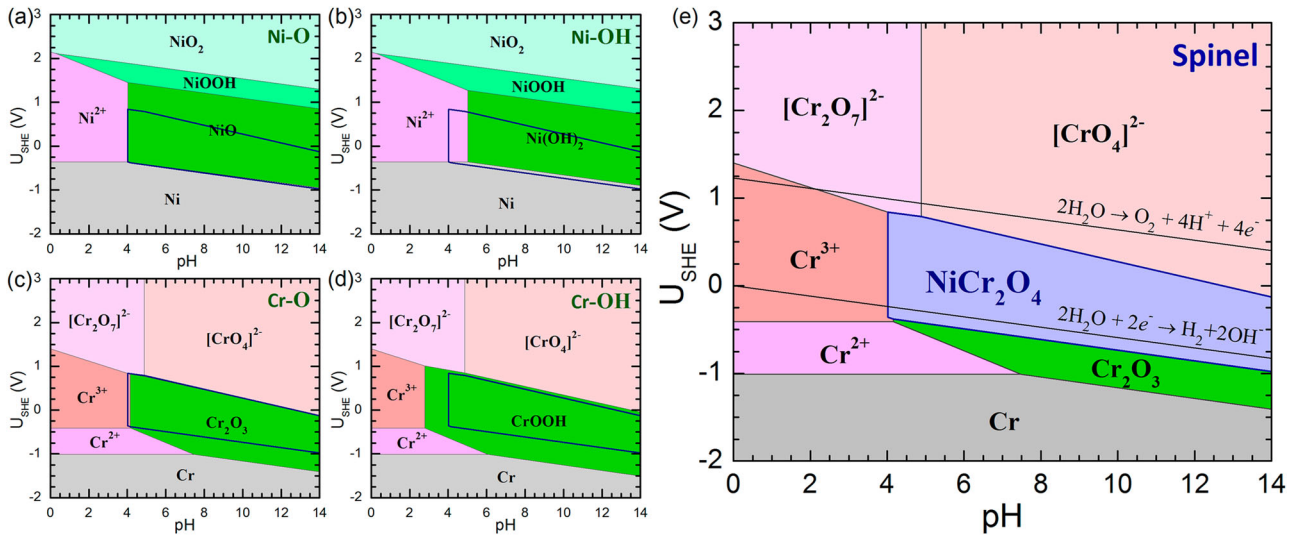

Fig. 6 First-principles Pourbaix diagrams (at 298.15 K, 1 bar, and $[I] = 10^{-4}$ M) for Ni–Cr alloys. The **a** Ni–O, (**b**) Ni-OH, (**c**) Cr-O, (**d**) Cr-OH, and (**e**) spinel subdiagrams present the phase domains of NiO, $Ni(OH)_2$, Cr_2O_3, CrOOH, and $NiCr_2O_4$, respectively. The phase domain of $NiCr_2O_4$ is also indicated by the blue boundary boxes in panels (**a**–**e**), and the equilibrium potentials for water oxidation and reduction are indicated by black lines in panel (**e**).

resultant oxide interfaces under various environments will be very important for better understanding/predicting the oxidation and corrosion behaviors and interphase dynamics, for which deeper studies are required in the future.

Apart from the passivating oxides with compact structures, the hydrated oxide products with less dense layered structures, e.g., $Ni(OH)_2$ and CrOOH, may inevitably form on top of the oxide/alloy surfaces in electrochemical conditions, owing to their large phase domains (high electrochemical stability) in the Ni–OH and Cr–OH diagrams (Fig. 6b, d). The phase domain areas for $Ni(OH)_2$ are just smaller than those of NiO, and those of CrOOH are even a little larger than those of Cr_2O_3. Such good stability makes them ubiquitously observed in various electrochemical experiments[20,37,39,40], and hydrated Cr oxides and Cr (oxy)hydroxides are frequently observed as the major electrochemical products[37,41,99,114,115], because of their higher stability than Cr_2O_3. These layered (oxy)hydroxides usually have a weak adhesion with the substrate alloys or oxide films and may even become suspended in solution. The wide interlayer openings in (oxy) hydroxide lattices are readily intercalated by environmental impurities[20,37,39,40], thus they poorly inhibit the attack of aggressive environmental agents. For the purpose of long-term passivation of Ni–Cr alloy surfaces, the growth of (oxy)hydroxides should be suppressed and/or that of denser oxides promoted. The alloying elements can be tuned to chemically activate the oxide formation[37,41,116,117], or to promote the nucleation of metastable Cr_2O_3 by providing a corundum structure template[118]. Some surface treatment methods can also be exploited to realize high-quality surface passivation, e.g., pre-oxidation in oxygen atmospheres[100,101] and deposition of oxide coatings[119].

Correlated Composition and Corrosion

The thermodynamic and electrochemical results from accurate first-principles calculations can be used to systematically understand the close relationship between composition, heat treatment, electrochemical oxidation, and dissolution for Ni–Cr alloys. The successful application of a Ni–Cr alloy should also rely on its intrinsic composition, fabrication treatments, and final interaction with working environments. Therefore, the thermodynamic and electrochemical knowledge established here can be combined to better understand the superior corrosion resistance of many existing alloys and then enable the design of improved Ni–Cr alloys with targeted stability.

We have mentioned above that the corrosion resistance of Cr_2O_3 is usually superior to NiO, because the former has lower defect migrations and surface reaction kinetics, which can be found from the monotonic decrease of polarization current in the passive region ($U = 0.5 - 1.0$ V) with increasing x_{Cr} of Ni–Cr alloys (Fig. 1b). We have also revealed above that it is the electrochemical driving force that can be controllable to induce the formation of a Cr_2O_3 layer on top of a NiO layer, which is an oxide-film morphology useful for the corrosion resistance of Ni–Cr alloys. According to the percolation theory established by Sieradzki et al.[23,24], a x_{Cr} above the critical value of 13 at.% is required for the formation of a homogeneous Cr_2O_3 network on Ni–Cr surface. Our first-principles thermodynamic calculations find an optimal range of x_{Cr} (14–34 at%) for obtaining the most stable Ni–Cr solid solutions under regular heat-treatment conditions (900–1500 K), which can quantitatively explain the empirical composition design for industrial Ni–Cr alloys. From a different perspective, i.e., electrochemical oxidation of an alloy, percolation theory establishes a similar lower limit of x_{Cr} (13 at%) for corrosion resistance of Ni–Cr alloys. Therefore, a x_{Cr} of $\gtrsim$13 at% should be employed for the design of more corrosion-resistant Ni–Cr alloys in the future, because of the simultaneously optimized thermodynamic and electrochemical stabilities required by both the fabrication treatments and realistic service.

For a Ni–Cr alloy with a high x_{Cr} (e.g., >30 at%), elemental partitioning can be initiated through a heat treatment such that the homogeneous solid solution spontaneously separates into lower-x_{Cr} (State I) and higher-x_{Cr} (State II) regions. Owing to the different work functions of pure γ-Ni (~5.2 eV) and α-Cr (~4.5 eV)[120], there may be an electron transfer from a higher-x_{Cr} region (anode) to the surrounding lower-x_{Cr} region (cathode). Such electron transfer will tend to bring the detrimental galvanic-corrosion effect[121] to the anodic Cr-rich regions. Fortunately, there will also be more Cr_2O_3 formed in the anodic regions, and the resultant higher degree of surface passivation can effectively reduce or even eliminate the galvanic corrosion. This detailed balance should naturally occur on Ni–Cr surfaces and will contribute to the high and long-standing corrosion resistance of Ni–Cr alloys. Furthermore, according to the appearance of lower-x_{Cr} regions caused by the elemental partitioning process, we expect that an upper limit for the global x_{Cr} may exist, above which the corrosion resistance may stop improving. The elemental-partitioning trends revealed here (Fig. 4c, d) can be used in part to determine the upper-limit x_{Cr} at 34 ± 3 at% (48 ± 4 at%) for the heat treatment at 900 K (1500 K).

Based on these analyses, favorable heat-treatment stability and qualified surface passivation require an x_{Cr} higher than 13–14 at%, and the minimized elemental partitioning during heat treatment at 900–1500 K prefers an average x_{Cr} lower than 34–48 at%. A stable solid-solution Ni–Cr structure allows the subsequent steady tuning of phases, grains, mechanical properties, and corrosion resistance by using other alloying additives and adopting appropriate heat treatments. The element Mo is usually added into industrial grades of Ni–Cr alloys (see Supplementary Table 2 for more details) to improve the corrosion resistance through many possible mechanisms (e.g., surface repassivation, defect transport suppression, Cr_2O_3-nucleation promotion, and trapping of corrosive Cl^- ions)[5,24,41,105,106,116,122,123]. From the perspective of electrochemical stability, the complex aqueous ions of Mo ($[MoO_4]^{2-}$ and $[HMoO_4]^-$) have especially low chemical potentials (−8.91 and −9.26 eV)[38], which results in high dissolubility of pure Mo metal and Mo-rich phase (Fig. 1d)[25]. Therefore, it is an important topic for first-principles simulations in the future to discern the corrosion-resistant effects at the atomic scale for soluble Mo in many important alloys (e.g., Ni–Cr alloys and steels) under different environmental conditions. For such theoretical studies, thermodynamic and electrochemical simulations should further join with kinetic simulation to both accurately determine the material states and yield many realistic material processes (e.g., current-potential polarization curves) that can be directly compared to or validated by experimental measurements[36,110,124–127].

SUMMARY REMARKS

In this work, an accurate first-principles simulation method has been employed to study the thermodynamic and electrochemical behaviors of Ni–Cr solid solutions. By combining a Debye model and DFT calculations with appropriately constructed random magnetism-structure configurations, we have systematically calculated and analyzed the composition- and temperature-dependent $\Delta_f G$ values of Ni–Cr alloys. This approach has led us to identify two important equilibrium states that can provide a quantitative explanation of the thermodynamic stability of Ni–Cr alloys. We have explained the thermodynamic driving force for elemental partitioning processes using these two equilibrium states and correlated many related experimental phenomena under different heat treatments. By employing a high-level DFT method that accounts for exact electronic exchange, we have calculated $\Delta_f G$ values of oxides and (oxy)hydroxides to construct reliable Pourbaix diagrams, which have been used to explain various experimental observations of oxide film growth and

corrosion phenomena on the alloy surfaces. We have further analyzed the correlation between elemental partitioning, heat-treatment temperature, surface passivation, and corrosion of Ni–Cr alloys based on the thermodynamic and electrochemical mechanisms established here. The thermodynamic and electrochemical principles we have identified for selecting optimal Ni–Cr alloy compositions both help us justify the conventional wisdom behind many industrial Ni–Cr alloys and further serve to guide the design of superior alloys with the desired corrosion resistance for service in other environments.

METHODS

DFT parameters

The DFT calculations are carried out using the Vienna Ab Initio Simulation (VASP) package[128], where the projector augmented-wave method[129,130] is implemented to express the electronic wavefunction and electron-ion interaction. The planewave cutoff energy is set to 600 eV, and the reciprocal k grids are $\gtrsim \frac{30}{a_0} \times \frac{30}{b_0} \times \frac{30}{c_0}$ for Ni–Cr alloys (a_0, b_0, and c_0 are lattice constants) and $\gtrsim \frac{20}{a_0} \times \frac{20}{b_0} \times \frac{20}{c_0}$ for the metal compounds (i.e., oxides, hydroxides, and oxyhydroxides), respectively. The self-consistent convergence thresholds for electronic energy, atomic force, and lattice stress are 10^{-7} eV, 10^{-3} eV Å^{-1}, and 0.5 kbar, respectively. The *Materials Project*[131], *Open Quantum Materials*[132], and *ICSD*[133] resources are used to obtain the initial atomic structures. Various magnetic configurations are screened for each structure to locate the most stable magnetic state[37]. The optimized structures and magnetic orders for binary-metal oxides ($NiCr_2O_4$ and $NiCrO_4$) are described in the Supplementary Information (see Section J), and those for mono-metal oxides and (oxy)hydroxides can be found in our prior work[37].

The spin-polarized semilocal PBE density functional[134] in the generalized gradient approximation is used to calculate the atomic structures, electronic structures, bulk moduli, and $\Delta_f G$ values of the Ni–Cr alloys. To accurately calculate the $\Delta_f G$ values of the metal compounds, it is necessary to mix nonlocal exact exchange (EXX) into the semilocal density functional[20,36]. The HSE06 type of hybrid functional[135,136], with 25% EXX replacing the PBE exchange potential (within an interaction range of 9.4 Å), is used to calculate the atomic structures and electronic energies for the metal compounds. The PBE functional is used to calculate the phonon spectra of Ni, Cr, and the considered compounds, where the atomic force constants are obtained by using the small-displacement method[37,137], and then the vibrational free energies are derived from the calculated phonon frequencies[63,64].

DATA AVAILABILITY

All the data needed to make the conclusions in this work have been provided in the manuscript and online Supplementary Information.

CODE AVAILABILITY

The VASP code package used in this work to carry out the DFT calculations can be obtained after a user license is authorized by the VASP company (https://www.vasp.at).

Received: 27 June 2023; Accepted: 24 November 2023;
Published online: 14 December 2023

REFERENCES

1. Padture, N. P., Gell, M. & Jordan, E. H. Thermal barrier coatings for gas-turbine engine applications. *Science* **296**, 280–284 (2002).
2. Clarke, D. & Levi, C. Materials design for the next generation thermal barrier coatings. *Annu. Rev. Mater. Res.* **33**, 383–417 (2003).
3. Luo, L. et al. Atomic origins of water-vapour-promoted alloy oxidation. *Nat. Mater.* **17**, 514–518 (2018).
4. Chen, Y., Zhao, X. & Xiao, P. Effect of microstructure on early oxidation of MCrAlY coatings. *Acta Mater.* **159**, 150–162 (2018).
5. Yu, X.-X. et al. Nonequilibrium solute capture in passivating oxide films. *Phys. Rev. Lett.* **121**, 145701 (2018).
6. Reynolds, T. et al. Identifying heating rate dependent oxidation reactions on a nickel-based superalloy using synchrotron diffraction. *Acta Mater.* **181**, 570–583 (2019).
7. Jafari, R. & Sadeghi, E. High-temperature corrosion performance of HVAF-sprayed NiCr, NiAl, and NiCrAlY coatings with alkali sulfate/chloride exposed to ambient air. *Corros. Sci.* **160**, 108066 (2019).
8. Moskal, G. et al. Microstructural characterization of laser-cladded NiCrAlY coatings on Inconel 625 Ni-based superalloy and 316L stainless steel. *Surf. Coat. Technol.* **387**, 125317 (2020).
9. Wang, K., Han, J., Gerard, A., Scully, J. & Zhou, B.-C. Potential-pH diagrams considering complex oxide solution phases for understanding aqueous corrosion of multi-principal element alloys. *npj Mater. Degrad.* **4**, 35 (2020).
10. Peng, J. et al. Data analytics approach to predict high-temperature cyclic oxidation kinetics of NiCr-based alloys. *npj Mater. Degrad.* **5**, 4 (2021).
11. Hu, Y. et al. Hot corrosion behavior of IN738LC alloy formed by selective laser melting. *Corros. Sci.* **198**, 110154 (2022).
12. Dash, A. et al. Recent advances in understanding diffusion in multiprincipal element systems. *Annu. Rev. Mater. Res.* **52**, 383–409 (2022).
13. Zinkle, S. J. & Busby, J. T. Structural materials for fission & fusion energy. *Mater. Today* **12**, 12–19 (2009).
14. Zinkle, S. & Snead, L. Designing radiation resistance in materials for fusion energy. *Annu. Rev. Mater. Res.* **44**, 241–267 (2014).
15. Lu, C. et al. Enhancing radiation tolerance by controlling defect mobility and migration pathways in multicomponent single-phase alloys. *Nat. Commun.* **7**, 13564 (2016).
16. Zhou, W. et al. Proton irradiation-decelerated intergranular corrosion of Ni-Cr alloys in molten salt. *Nat. Commun.* **11**, 3430 (2020).
17. Terrani, K. A. Accident tolerant fuel cladding development: promise, status, and challenges. *J. Nucl. Mater.* **501**, 13–30 (2018).
18. Ma, H.-B. et al. Oxidation behavior of Cr-coated zirconium alloy cladding in high-temperature steam above 1200 °C. *npj Mater. Degrad.* **5**, 7 (2021).
19. Cui, L. et al. TEM characterization of irradiation-induced dislocation loops and voids in ion-irradiated pure chromium. *J. Nucl. Mater.* **569**, 153920 (2022).
20. Huang, L.-F. & Rondinelli, J. M. Electrochemical phase diagrams of Ni from ab initio simulations: role of exchange interactions on accuracy. *J. Phys.* **29**, 475501 (2017).
21. Sun, T.-Y., Hao, Y., Lin, C.-T., Wang, L. & Huang, L.-F. Unraveling the strong coupling between graphene/nickel interface and atmospheric adsorbates for versatile realistic applications. *Carbon Trends* **2**, 100013 (2021).
22. Miller, C., Field, R. & Kaufman, M. Phase stability of γ'-Ni_2Cr and α-Cr in the Ni-Cr binary. *Acta Mater.* **157**, 1–10 (2018).
23. Xie, Y. et al. A percolation theory for designing corrosion-resistant alloys. *Nat. Mater.* **20**, 789–793 (2021).
24. Williams, D. E., Newman, R. C., Song, Q. & Kelly, R. G. Passivity breakdown and pitting corrosion of binary alloys. *Nature* **350**, 216–219 (1991).
25. Duarte, M. J. et al. Element-resolved corrosion analysis of stainless-type glass-forming steels. *Science* **341**, 372–376 (2013).
26. Tso, N. C., Kosugi, M. & Sanchez, J. M. The effect of the structural energy of Cr on the Ni-Cr equilibrium phase diagram. *Acta Metall.* **37**, 121–127 (1989).
27. Udovsky, A. L. & Kozodaeva, E. A. An optimized calculation of phase diagram and thermodynamic properties of the Ni-Cr system. *Calphad* **17**, 17–34 (1993).
28. Tang, F. & Hallstedt, B. Using the PARROT module of Thermo-Calc with the Cr-Ni system as example. *Calphad* **55**, 260–269 (2016).
29. Hao, L., Ruban, A. & Xiong, W. CALPHAD modeling based on Gibbs energy functions from zero Kevin and improved magnetic model: a case study on the Cr-Ni system. *Calphad* **73**, 102268 (2021).
30. Craievich, P. J., Sanchez, J. M., Watson, R. E. & Weinert, M. Structural instabilities of excited phases. *Phys. Rev. B* **55**, 787–797 (1997).
31. Craievich, P. J. & Sanchez, J. M. Vibrational free energy in the Ni-Cr system. *Comput. Mater. Sci.* **8**, 92–99 (1997).
32. Breidi, A., Fries, S., Palumbo, M. & Ruban, A. First-principles modeling of energetic and mechanical properties of Ni-Cr, Ni-Re and Cr-Re random alloys. *Comput. Mater. Sci.* **117**, 45–53 (2016).
33. Zhang, J., Korzhavyi, P. A. & He, J. First-principles modeling of solute effects on thermal properties of nickel alloys. *Mater. Today Commun.* **28**, 102551 (2021).
34. Xiong, Z. et al. Accelerating optimization of IN718 by mapping alloying effects on phase stabilities and mechanical properties using high-throughput calculations. *Mater. Des.* **217**, 110603 (2022).

35. Zhang, J., Korzhavyi, P. A. & He, J. First-principle investigation of the stability and mechanical properties of the binder phase B (B=Co and Ni) with the maximum solubility of the transition-group elements M (M=V, Ti, Ta, Mo, W and Cr). *Mater. Today Commun.* **34**, 105217 (2023).
36. Huang, L.-F., Scully, J. R. & Rondinelli, J. M. Modeling corrosion with first-principles electrochemical phase diagrams. *Ann. Rev. Mater. Res.* **49**, 53–77 (2019).
37. Huang, L.-F. & Rondinelli, J. M. Reliable electrochemical phase diagrams of magnetic transition metals and related compounds from high-throughput ab initio calculations. *npj Mater. Degrad.* **3**, 26 (2019).
38. Pourbaix, M. *ATLAS of Electrochemical Equilibria in Aqueous Solutions* (Pergamon Press, Oxford, 1966).
39. Huang, L. F., Hutchison, M. J., Santucci Jr, R. J., Scully, J. R. & Rondinelli, J. M. Improved electrochemical phase diagrams from theory and experiment: The Ni-water system and its complex compounds. *J. Phys. Chem. C* **121**, 9782–9789 (2017).
40. Huang, L.-F., Ha, H. M., Lutton Cwalina, K., Scully, J. R. & Rondinelli, J. M. Understanding electrochemical stabilities of Ni-based nanofilms from a comparative theory-experiment approach. *J. Phys. Chem. C* **123**, 28925–28940 (2019).
41. Lutton Cwalina, K. et al. In Operando analysis of passive film growth on Ni-Cr and Ni-Cr-Mo alloys in chloride solutions. *J. Electrochem. Soc.* **166**, C3241–C3253 (2019).
42. Sabatini, M., Monaco, L. & Erb, U. Corrosion of nanocrystalline and coarse-grained nickel-iron (Ni-Fe) alloys in neutral and alkaline sulfate environments. *Corros. Sci.* **163**, 108233 (2020).
43. Langley, A. R., Elmer, A., Fletcher, P. J. & Marken, F. Linking the Cu(II/I) and the Ni(IV/II) potentials to subsequent passive film breakdown for a Cu-Ni alloy in aqueous 0.5 M NaCl. *ChemElectroChem* **7**, 195–200 (2020).
44. Han, J. et al. Potential dependent Mn oxidation and its role in passivation of $Ni_{38}Fe_{20}Cr_{22}Mn_{10}Co_{10}$ multi-principal element alloy using multi-element resolved atomic emission spectroelectrochemistry. *J. Electrochem. Soc.* **168**, 051508 (2021).
45. Fu, H. J. et al. Catalytic open-circuit passivation by thin metal oxide films of p-Si anodes in aqueous alkaline electrolytes. *Energy Environ. Sci.* **15**, 334–345 (2022).
46. Bak, J., Bae, H. B. & Chung, S.-Y. Atomic-scale perturbation of oxygen octahedra via surface ion exchange in perovskite nickelates boosts water oxidation. *Nat. Commun.* **10**, 2713 (2019).
47. Chatti, M. et al. Intrinsically stable in situ generated electrocatalyst for long-term oxidation of acidic water at up to 80 °C. *Nat. Catal.* **2**, 457–465 (2019).
48. Moysiadou, A. & Hu, X. Stability profiles of transition metal oxides in the oxygen evolution reaction in alkaline medium. *J. Mater. Chem. A* **7**, 25865–25877 (2019).
49. Ros, C., Andreu, T., David, J., Arbiol, J. & Morante, J. R. Degradation and regeneration mechanisms of NiO protective layers deposited by ALD on photoanodes. *J. Mater. Chem. A* **7**, 21892–21902 (2019).
50. Kou, T. et al. Carbon doping switching on the hydrogen adsorption activity of NiO for hydrogen evolution reaction. *Nat. Commun.* **11**, 590 (2020).
51. Buchele, S. et al. Structure sensitivity and evolution of nickel-bearing nitrogen-doped carbons in the electrochemical reduction of CO_2. *ACS Catal.* **10**, 3444–3454 (2020).
52. Kim, H. et al. Identification of single-atom Ni site active toward electrochemical CO_2 conversion to CO. *J. Am. Chem. Soc.* **143**, 925–933 (2021).
53. Feng, C. et al. A self-healing catalyst for electrocatalytic and photoelectrochemical oxygen evolution in highly alkaline conditions. *Nat. Commun.* **12**, 5980 (2021).
54. Zhou, Y. et al. Long-chain hydrocarbons by CO_2 electroreduction using polarized nickel catalysts. *Nat. Catal.* **5**, 545–554 (2022).
55. Beinlich, A. et al. Peridotite weathering is the missing ingredient of Earth's continental crust composition. *Nat. Commun.* **9**, 634 (2018).
56. Schieber, J. et al. Mars is a mirror—understanding the Pahrump Hills mudstones from a perspective of Earth analogues. *Sedimentology* **69**, 2371–2435 (2022).
57. van de Walle, A. & Ceder, G. The effect of lattice vibrations on substitutional alloy thermodynamics. *Rev. Mod. Phys.* **74**, 11–45 (2002).
58. Nagasako, N., Jahnátek, M., Asahi, R. & Hafner, J. Anomalies in the response of V, Nb, and Ta to tensile and shear loading: ab initio density functional theory calculations. *Phys. Rev. B* **81**, 094108 (2010).
59. Nagasako, N., Asahi, R. & Hafner, J. Ideal tensile and shear strength of a gum metal approximant: ab initio density functional calculations. *Phys. Rev. B* **85**, 024122 (2012).
60. Grimvall, G., Magyari-Köpe, B., Ozoliņš, V. & Persson, K. A. Lattice instabilities in metallic elements. *Rev. Mod. Phys.* **84**, 945–986 (2012).
61. Huang, L.-F., Grabowski, B., McEniry, E., Trinkle, D. R. & Neugebauer, J. Importance of coordination number and bond length in titanium revealed by electronic structure investigations. *Phys. Status Solidi B* **252**, 1907–1924 (2015).
62. Wróbel, J. S., Nguyen-Manh, D., Lavrentiev, M. Y., Muzyk, M. & Dudarev, S. L. Phase stability of ternary fcc and bcc Fe-Cr-Ni alloys. *Phys. Rev. B* **91**, 024108 (2015).
63. Wang, Y., Liu, Z.-K. & Chen, L.-Q. Thermodynamic properties of Al, Ni, NiAl, and Ni_3Al from first-principles calculations. *Acta Mater.* **52**, 2665–2671 (2004).
64. Huang, L.-F., Lu, X.-Z., Tennessen, E. & Rondinelli, J. M. An efficient ab-initio quasiharmonic approach for the thermodynamics of solids. *Comput. Mater. Sci.* **120**, 84–93 (2016).
65. Zhuang, J., Wang, H., Zhang, Q. & Wentzcovitch, R. M. Thermodynamic properties of ϵ-Fe with thermal electronic excitation effects on vibrational spectra. *Phys. Rev. B* **103**, 144102 (2021).
66. Yeh, J.-W. et al. Nanostructured high-entropy alloys with multiple principal elements: Novel alloy design concepts and outcomes. *Adv. Eng. Mater.* **6**, 299–303 (2004).
67. Chase, M. W. *NIST-JANAF Thermochemical Tables (4th Ed.)* (American Institute of Physics, New York, 1998).
68. Glensk, A., Grabowski, B., Hickel, T. & Neugebauer, J. Understanding anharmonicity in fcc materials: From its origin to ab initio strategies beyond the quasiharmonic approximation. *Phys. Rev. Lett.* **114**, 195901 (2015).
69. Körmann, F., Hickel, T. & Neugebauer, J. Influence of magnetic excitations on the phase stability of metals and steels. *Curr. Opin. Solid State Mater. Sci.* **20**, 77–84 (2016).
70. Gong, Y. et al. Temperature dependence of the Gibbs energy of vacancy formation of fcc Ni. *Phys. Rev. B* **97**, 214106 (2018).
71. Moruzzi, V. L., Janak, J. F. & Schwarz, K. Calculated thermal properties of metals. *Phys. Rev. B* **37**, 790–799 (1988).
72. Blanco, M., Francisco, E. & Luana, V. GIBBS: isothermal-isobaric thermodynamics of solids from energy curves using a quasi-harmonic Debye model. *Comput. Phys. Commun.* **158**, 57–72 (2004).
73. Shang, S. & Böttger, A. A combined cluster variation method and ab initio approach to the γ-Fe[N]/$\gamma\prime$-Fe_4N_{1-x} phase equilibrium. *Acta Mater.* **53**, 255–264 (2005).
74. Mei, Z.-G., Shang, S.-L., Wang, Y. & Liu, Z.-K. Density-functional study of the thermodynamic properties and the pressure–temperature phase diagram of Ti. *Phys. Rev. B* **80**, 104116 (2009).
75. Shang, S.-L., Wang, Y., Kim, D. & Liu, Z.-K. First-principles thermodynamics from phonon and Debye model: Application to Ni and Ni_3Al. *Comput. Mater. Sci.* **47**, 1040–1048 (2010).
76. Poirier, J. P. *Introduction to the Physics of the Earth's Interior*. Introduction to the Physics of the Earth's Interior (Cambridge University Press, Cmbridge, 2000).
77. Maisel, S. B., Höfler, M. & Müller, S. A canonical stability-elasticity relationship verified for one million face-centered-cubic structures. *Nature* **491**, 740–744 (2012).
78. Speich, G. R., Schwoeble, A. J. & Leslie, W. C. Elastic constants of binary iron-base alloys. *Metall. Mater. Trans. B* **3**, 2031–2037 (1972).
79. Weston, W. F., Ledbetter, H. M. & Naimon, E. R. Dynamic low-temperature elastic properties of two austenitic nickel-chromium-iron alloys. *Mater. Sci. Eng.* **20**, 185 – 194 (1975).
80. Weston, W. F. & Ledbetter, H. M. Low-temperature elastic properties of a nickel-chromium-iron-molybdenum alloy. *Mater. Sci. Eng.* **20**, 287 – 290 (1975).
81. Prokofev, D. I. & Fedotov, S. G. Elastic properties of maraging steels. *Met. Sci. Heat Treat.* **17**, 171–173 (1975).
82. Piatti, G. & Schiller, P. Thermal and mechanical properties of the Cr-Mn-(Ni-free) austenitic steels for fusion reactor applications. *J. Nucl. Mater.* **141-143**, 417 – 426 (1986).
83. Ledbetter, H. M. & Kim, S. A. Molybdenum effect on Fe-Cr-Ni-alloy elastic constants. *J. Mater. Res.* **3**, 40–44 (1988).
84. Duffy, T. S. & Ahrens, T. J. Dynamic compression of an Fe-Cr-Ni alloy to 80 GPa. *J. Appl. Phys.* **82**, 4259–4269 (1997).
85. Gao, M. C. et al. Phase stability and elastic properties of Cr-V alloys. *J. Phys.* **25**, 075402 (2013).
86. Arshed, M. & Butt, N. M. Temperature dependence of Mössbauer spectra. *Phys. Stat. Sol. A* **148**, K93–K97 (1995).
87. Teklu, A., Ledbetter, H., Boatner, L. A., McGuire, M. & Keppens, V. Single-crystal elastic constants of Fe-15Ni-15Cr alloy. *Metall. Mater. Trans. A* **35**, 3149–3154 (2004).
88. Khan, S. A., Ziya, A. B., Atiq, S. & Aziz, A. A study of the structure and thermal parameters of $Ni_{88.6}Cr_{11.4}$ alloy. *Phys. Scr.* **84**, 065603 (2011).
89. Gurrappa, I. Identification of hot corrosion resistant MCrAlY based bond coatings for gas turbine engine applications. *Surf. Coat. Technol.* **139**, 272–283 (2001).
90. Jackson, R., Taylor, M., Evans, H. & Li, X. Oxidation study of an EB-PVD MCrAlY thermal barrier coating system. *Oxid. Met.* **76**, 259–271 (2011).
91. Liu, X. et al. Hot corrosion behavior of NiCoCrAlYTa coating deposited on Inconel alloy substrate by high velocity oxy-fuel spraying upon exposure to molten V_2O_5-containing salts. *Corros. Sci.* **112**, 696–709 (2016).
92. Kalush, A. et al. Size effects on high temperature oxidation of MCrAlY coatings processed via APS and HVOF depositions. *Surf. Coat. Technol.* **440**, 128483 (2022).

93. Wang, Q. et al. Oxidation and hot corrosion behaviors of Mo-doped NiMoAlY alloys at 750 °C. *Corros. Sci.* **201**, 110262 (2022).
94. Bard, A. J., Parsons, R. & Jordan, J. *Standard Potentials in Aqueous Solution* (Marcel Dekker, New York, 1985).
95. Kubaschewski, O., Alcock, C. B. & Spencer, P. J. *Materials Thermochemistry* (Pergamon Press, Oxford, 1993).
96. Muller, O., Roy, R. & White, W. B. Phase equilibria in the systems NiO-Cr_2O_3-O_2, MgO-Cr_2O_3-O_2, and CdO-Cr_2O_3-O_2 at high oxygen pressures. *J. Am. Ceram. Soc.* **51**, 693–699 (1968).
97. Stefanecu, M., Barbu, M., Barvinschi, P. & Stefanescu, O. The obtaining of $NiCr_2O_4$ nanoparticles by unconventional synthesis methods. *J. Therm. Anal. Calorim.* **111**, 1121–1127 (2013).
98. Luo, L. et al. In-situ transmission electron microscopy study of surface oxidation for Ni–10Cr and Ni–20Cr alloys. *Scr. Mater.* **114**, 129–132 (2016).
99. Maurice, V. & Marcus, P. Progress in corrosion science at atomic and nanometric scales. *Prog. Mater. Sci.* **95**, 132–171 (2018).
100. Blades, W. H. & Reinke, P. From alloy to oxide: capturing the early stages of oxidation on Ni-Cr(100) Alloys. *ACS Appl. Mater. Interfaces* **10**, 43219–43229 (2018).
101. Blades, W. H., Barone, M. R. & Reinke, P. Initial atomic-scale oxidation pathways on a Ni-15Cr(100) alloy surface. *npj Mater. Degrad.* **5**, 17 (2021).
102. Ru, X. et al. Effects of iron content in NiCrFe alloys on the oxide films formed in an oxygenated simulated PWR water environment. *J. Nucl. Mater.* **509**, 29–42 (2018).
103. Oh, K., Ahn, S., Eom, K., Jung, K. & Kwon, H. Observation of passive films on Fe-20Cr-*x*Ni ($x = 0, 10, 20$ wt.%) alloys using TEM and Cs-corrected STEM-EELS. *Corros. Sci.* **79**, 34–40 (2014).
104. Hamada, E. et al. Direct imaging of native passive film on stainless steel by aberration corrected STEM. *Corros. Sci.* **52**, 3851–3854 (2010).
105. Zhang, B. et al. Unmasking chloride attack on the passive film of metals. *Nat. Commun.* **9**, 2559 (2018).
106. Zhang, B. et al. Chloride attack on the passive film of duplex alloy. *Corros. Sci.* **154**, 123–128 (2019).
107. Mortazavi, A. et al. Exploring failure modes of alumina scales on FeCrAl and FeNiCrAl alloys in a nitriding environment. *Acta Mater.* **201**, 131–146 (2020).
108. Wang, S. et al. Atomic scale mechanisms of multimode oxide growth on nickel-chromium alloy: direct in situ observation of the initial oxide nucleation and growth. *ACS Appl. Mater. Interfaces* **13**, 1903–1913 (2021).
109. Kovalov, D., Ghanbari, E., Mao, F., Kursten, B. & Macdonald, D. D. Investigation of artificial pit growth in carbon steel in highly alkaline solutions containing 0.5 M NaCl under oxic and anoxic conditions. *Electrochim. Acta* **320**, 134554 (2019).
110. Hao, Y., Wang, L. & Huang, L.-F. Lanthanide-doped MoS_2 with enhanced oxygen reduction activity and biperiodic chemical trends. *Nat. Commun.* **14**, 3256 (2023).
111. Huang, L., Sun, X., Guan, H. & Hu, Z. Oxidation behavior of a single-crystal Ni-base superalloy in air at 900, 1000 and 1100 °C. *Oxid. Met.* **65**, 207–222 (2006).
112. Pei, J. et al. Microstructure-dependent oxidation behavior of Ni-Al single-crystal alloys. *J. Mater. Sci. Technol.* **52**, 162–171 (2020).
113. Calvarin, G., Molins, R. & Huntz, A. Oxidation mechanism of Ni-20Cr foils and its relation to the oxide-scale microstructure. *Oxid. Met.* **53**, 25–48 (2000).
114. Li, Y. et al. Early oxidation mechanism of austenitic stainless steel TP347H in supercritical water. *Corros. Sci.* **128**, 241–252 (2017).
115. Sun, B., Zuo, X., Cheng, X. & Li, X. The role of chromium content in the long-term atmoshperic corrosion process. *npj Mater. Degrad.* **4**, 37 (2020).
116. Li, X. et al. The contribution of Cr and Mo to the passivation of Ni22Cr and Ni22Cr10Mo alloys in sulfuric acid. *Corros. Sci.* **176**, 109015 (2020).
117. Volders, C. et al. Unraveling the role of tungsten as a minor alloying element in the oxidation NiCr alloys. *npj Mater. Degrad.* **6**, 52 (2022).
118. Grabke, H. Oxidation of NiAl and FeAl. *Intermetallics* **7**, 1153–1158 (1999).
119. Zhang, X. et al. Al_2O_3-modified PS-PVD 7YSZ thermal barrier coatings for advanced gas-turbine engines. *npj Mater. Degrad.* **4**, 31 (2020).
120. Lide, D. R. & Haynes, W. M. *CRC Handbook of Chemistry and Physics (90th Edition)* (Taylor and Francis, Boca Raton, FL, 2010).
121. Wu, Y., Sun, T.-Y., Ge, T., Zhao, W. & Huang, L.-F. Eliminating the galvanic corrosion effect of graphene coating by an accurate and rapid self-assembling defect healing approach. *Adv. Funct. Mater.* **32**, 2110264 (2022).
122. Ryan, M., Williams, D., Chater, R., Hutton, B. & McPhall, D. Why stainless steel corrodes. *Nature* **415**, 770–774 (2002).
123. Punckt, C. et al. Sudden onset of pitting corrosion on stainless steel as a critical phenomenon. *Science* **305**, 1133–1136 (2004).
124. Todorova, M. & Neugebauer, J. Extending the concept of defect chemistry from semiconductor physics to electrochemistry. *Phys. Rev. Appl.* **1**, 014001 (2014).
125. Surendralal, S., Todorova, M. & Neugebauer, J. Impact of water coadsorption on the electrode potential of H-Pt(111)-liquid water interfaces. *Phys. Rev. Lett.* **126**, 166802 (2021).
126. Sun, H. et al. First-principles modeling of the anodic and cathodic polarization to predict the corrosion behavior of Mg and its alloys. *Acta Mater.* **244**, 118562 (2023).
127. Ma, G. et al. Mn-doped NiCoP nanopin arrays as high-performance bifunctional electrocatalysts for sustainable hydrogen production via overall water splitting. *Nano Energy* **115**, 108679 (2023).
128. Hafner, J. Ab-initio simulations of materials using VASP: density-functional theory and beyond. *J. Comput. Chem.* **29**, 2044 – 2078 (2008).
129. Blöchl, P. E. Projector augmented-wave method. *Phys. Rev. B* **50**, 17953–17979 (1994).
130. Kresse, G. & Joubert, D. From ultrasoft pseudopotentials to the projector augmented-wave method. *Phys. Rev. B* **59**, 1758–1775 (1999).
131. Jain, A. et al. The Materials Project: a materials genome approach to accelerating materials innovation. *APL Mater.* **1**, 011002 (2013).
132. Saal, J., Kirklin, S., Aykol, M., Meredig, B. & Wolverton, C. Materials design and discovery with high-throughput density functional theory: The Open Quantum Materials Database (OQMD). *JOM* **65**, 1501–1509 (2013).
133. Belsky, A., Hellenbrandt, M., Karen, V. L. & Luksch, P. New developments in the Inorganic Crystal Structure Database (ICSD): accessibility in support of materials research and design. *Acta Crystallogr. Sect. B* **58**, 364–369 (2002).
134. Perdew, J. P., Burke, K. & Ernzerhof, M. Generalized gradient approximation made simple. *Phys. Rev. Lett.* **77**, 3865–3868 (1996).
135. Heyd, J., Scuseria, G. E. & Ernzerhof, M. Erratum: "Hybrid functionals based on a screened Coulomb potential" [J. Chem. Phys.118, 8207 (2003)]. *J. Chem. Phys.* **124**, 219906 (2006).
136. Vydrov, O. A., Heyd, J., Krukau, A. V. & Scuseria, G. E. Importance of short-range versus long-range Hartree-Fock exchange for the performance of hybrid density functionals. *J. Chem. Phys.* **125**, 074106 (2006).
137. Togo, A. & Tanaka, I. First principles phonon calculations in materials science. *Scr. Mater.* **108**, 1–5 (2015).

ACKNOWLEDGEMENTS

The authors thank Dr. Sascha B. Maisel at Max-Planck-Institut für Eisenforschung GmbH for sending all the original data on the stiffness-stability relationships for many kinds of alloys (Ni–Ta, Ni–W, Ni–Al, and Cu–Al) reported in his prior work[77], as well as Professor Blazej Grabowski at the University of Stuggart for coordinating such helpful exchange. L.-F.H. is sponsored by the Fund of Science and Technology on Surface Physics and Chemistry Laboratory (Grant No. XKFZ202101) and the National Natural Science Foundation of China (Grant Nos. U21A20127 and 22272192). J.M.R. and K.S. were supported by the National Science Foundation (NSF) under award numbers DMR-2208865 and DMR-2208848. Calculations were performed using the QUEST HPC facility at Northwestern University and the Supercomputing Center at Ningbo Institute of Materials Technology and Engineering, Chinese Academy of Sciences.

AUTHOR CONTRIBUTIONS

L.-F.H. and J.M.R. conceived the theoretical idea, designed the computational methods, and performed the ab initio calculations. Y.X. and K.S. performed related experiments on Ni–Cr alloys. All of the authors participated in the formal analysis and manuscript writing. L.-F.H., J.M.R., and K.S. acquired the necessary resources. J.M.R. supervised the project.

COMPETING INTERESTS

The authors declare no competing interests.

ADDITIONAL INFORMATION

Supplementary information The online version contains supplementary material available at https://doi.org/10.1038/s41529-023-00414-w.

Correspondence and requests for materials should be addressed to James M. Rondinelli.